Revision 1

Crystal structures, and high-temperature and high-pressure vibrational spectra of synthetic fluorine-bearing brucites

Yunfan Miao[1], Xi Zhu[1], Yu Ye[1]*, Joseph R. Smyth[2], Dan Liu[1], Yancheng Hu[1], Guangchen Chen[1]

[1]State Key Laboratory of Geological Processes and Mineral Resources, China University of Geosciences, Wuhan, 430074, China

[2]Department of Geological Sciences, University of Colorado, Boulder, Colorado, 80309, USA

*Contacting email: yeyu@cug.edu.cn

Abstract: Brucite ($Mg(OH)_2$) has been extensively studied as a simple and important analog for physical and chemical properties of hydrous minerals, and fluorine substitution ($OH^- = F^-$) is common in hydrous minerals since the radius of F^- is similar to that of O^{2-}. We synthesized two F-bearing brucite samples, $Mg(OH)_{1.78}F_{0.22}$ and $Mg(OH)_{1.16}F_{0.84}$, at 9.5 GPa and 1373 K. Single-crystal X-ray diffraction measurements indicate that both the phases still crystallize in the space group of $P3m1$, and fluorine substitution significantly reduces the unit cell volume, axial lengths, and averaged Mg-O(F) bond lengths. The averaged O…H distances get slightly shortened and the H-O-H angles become smaller due to the fluorine effect. Additional IR-active OH-stretching bands are observed at 3660, 3644, and 3513 cm^{-1} for the F-bearing samples, besides the original one at 3695 cm^{-1}. *In situ* high-temperature and high-pressure Raman and Fourier transform infrared (FTIR) spectra were collected on the F-bearing brucite samples and comparisons are made with the natural one with 0.7 mol.% F^-. The temperature dependence ($(\partial v_i/\partial T)_P$) of the OH-stretching modes is inversely correlated to the vibrational frequencies from 3500 to 3700 cm^{-1}, whereas $(\partial v_i/\partial P)_T$ is in positive correlation with v_i. In addition, the dehydration points in the F-bearing brucites are 100 – 150 K higher than that for the F-free sample at the ambient pressure. By creating new proton positions in lower energies, fluorine substitution stabilizes hydrous minerals (like brucite) to higher temperatures and significantly affects their thermodynamic properties, which has significant implications in mineral physical and geochemical studies.

Keywords: brucite; fluorine substitution; crystal structure; high-temperature Raman spectra; high-pressure FTIR spectra; OH-stretching mode

1. Introduction

Brucite (Mg $(OH)_2$ with 31 wt% H_2O) has been extensively studied as a most important analog for dense hydrous minerals in the peridotite (MgO-SiO_2-$Mg(OH)_2$) system, like the serpentine-group minerals, phases A, E and D, supper-hydrous phase B, and the humite-group minerals on the olivine – brucite join (Wunder 1998), all of which are important H_2O carriers in the deep Earth interior. Besides, brucite is a building block for phyllosilicates including clay minerals. The thermodynamic properties of the brucite-group minerals have many significant applications in both mineral physics and geochemistry, such as equations of state (Fei and Mao 1993; Parise 1994; Catti et al. 1995; Fukui et al. 2003; Xu et al. 2007a; Horita et al. 2010), thermoelasticity (Xia et al. 1998; Jiang et al. 2006), dehydration at high P-T conditions ((Kanzaki 1991; Liu 2018), hydrogen isotopic effect on the crystal structures (Xu et al. 2007b, 2013; Chakoumakos et al. 2013), and equilibrium D/H fractionation in the brucite-water system at various *P-T* conditions (Satake and Matsuo 1984; Saccocia et al. 1998; Xu and Zheng 1999; Horita et al. 2002, 2018; Méheut et al. 2007, 2010; Reynard and Caracas 2009).

On the other hand, fluorine is the most abundant halogen element in the mantle, most of which could be carried into the deep mantle by subduction slabs (e.g. McDonough and Sun, 1995; Straub and Layne 2003; Pagé and Hattori 2019). Since, the radius of F^- is quite close to that for O^{2-} (Shannon 1976), the OH^- = F^- substitution is very common in hydrous minerals, like serpentines, micas, as well as the humite-group minerals including chondrodite and clinohumite (e.g. Ottolini et al. 2000; Lin et al. 1999, 2000; Liu et al. 2019, 2021). Fluorine substitution can stabilize hydrous minerals to significantly higher temperatures in subduction zones as well as in the whole mantle, like clinohumite (Grützner et al. 2017).

In this study, we will synthesize F-bearing brucite samples in a multi-anvil press and investigate the fluorine substitution mechanism in the brucite crystal structure. Since the internal OH-stretching vibrations play a crucial role in determining the thermodynamic properties at high *P-T* conditions (e.g. Reynard and Caracas 2009; Ma et al. 2013; Zhu et al. 2019), *in situ* high-temperature and high-pressure Raman and FTIR spectra will be measured on these F-bearing samples. It is important for us to have a systematic investigation of the fluorine effect on hydrogen behavior in the minerals, such as brucite, at various *P-T* conditions, which are essential for constraining the physical and chemical properties of hydrous minerals in the presence of fluorine. Hence, the synthetic F-bearing brucite samples should be useful analogs for studying volatile cycling (for both water and fluorine) in the Earth's system.

2. Experimental methods and results

2.1. Sample synthesis and chemical analysis

Two fluorine-bearing brucite samples were synthesized using the 1000-ton multi-anvil press at State Key Laboratory of Geological Processes and Mineral Resources, China University of Geosciences, Wuhan. Two mixtures were prepared in the molar ratios of MgF_2 : $Mg(OH)_2$ equal to 1 : 9 and 2 : 3, respectively, and both the starting materials of MgF_2 and $Mg(OH)_2$ are analytical reagents with purities > 99.9 % (purchased from Alfa Aesar). The mixtures were loaded in two welded platinum capsules (length: 2 mm, outer diameter: 2 mm and thickness: 0.2 mm), and we adopted 14-mm periclase octahedra and 25.4-mm tungsten carbide anvils with 8-mm corner truncations (i.e. 14/8 assemblages). According to the reported phase equilibrium relation in the $MgO-H_2O$ system (Fei and Mao 1993), the stable temperature for brucite reaches maximum of approximately 1473 K, in a narrow pressure range of 8 to 11 GPa, while it would break into MgO and liquid H_2O at higher temperatures. Hence, these synthetic experiments were designed at the *P-T* condition of 9.5 GPa and 1373 K, with a duration of 12 hours. The temperature was monitored with a C-type (W5Re95-W2Re74) thermocouple, and graphite furnaces were utilized in this experiment. The microphotograph of a recovered sample chip (with the starting composition of MgF_2 : $Mg(OH)_2$ = 2 : 3) is shown in **Fig. S1** in the supplementary materials.

For chemical analysis, we selected 3 chips (with diameters of 80 – 120 μm) from each of the synthetic sample sources, as well as one grain (with a diameter of approximately 200 μm) of a natural brucite sample from Emei Mountain, China. All these grains were mounted in epoxy and polished on the surfaces. The chemical compositions were characterized by a JEOL JXA-8100 Electron Probe Micro Analyzer (EPMA), which is equipped with four wavelength-dispersive spectrometers (WDS). This system was operated at an accelerating voltage of 15 kV and a beam current of 20 nA, and the spot size was reduced to 5 nm to minimize the fluctuations of X-ray intensity as well as the damage on the sample (Wang et al. 2019). Certified mineral standards were used (periclase for Mg, apatite for F) for quantification using ZAF wavelength-dispersive corrections. Peak counting times were 20 s for Mg and F. For each of these three brucite samples, 12 to 15 points were chosen for measuring the weight percentages of MgO and F^-, and the averaged values with standard deviations are listed in **Table 1**. The measured MgO weight percentages stand for the total Mg amount including MgF_2 with the conversion of MgF_2 = MgO, and the F^- weight percentages have already been calculated for the anion alone. Hence, the formulae for the synthetic samples R1201 and R1202 can be interpreted as $Mg(OH)_{1.784}F_{0.216}$ and $Mg(OH)_{1.156}F_{0.844}$, respectively, which are quite consistent with the starting mixture. The composition of the natural brucite sample is $Mg(OH)_{1.986}F_{0.014}$, suggesting that 0.7 % of OH^- is substituted by F^-.

2.2. Single-crystal X-ray diffraction (XRD)

Three single crystals (with diameters of approximately 100 μm) were selected for the single-crystal XRD at ambient conditions on a Rigaku XtalAB mini diffractometer (Rigaku, Japan) (Miao et al. 2019). The analyzer was equipped with a 600-w rotating Mo-anode X-ray source and a Saturn 724 HG CCD detector (with a resolution of 1024×1024), and the X-ray source was operated at a voltage of 50 kV and a current of 20 mA. We collected the intensity data in a 2θ scanning range of up to 52°, and the averaged wavelength of Mo $K_{\alpha1}$-$K_{\alpha2}$ was calibrated to 0.71073 Å (Wang et al. 2020). The intensity data collection and refined unit-cell parameters are listed in **Table 2**.

The atomic positions (**Table 3**) and anisotropic displacement parameters (**Table S1** in the supplementary materials) were refined using the program SHELXL (Sheldrick 2015) in the software package of CrysAlisPro/Olex2 (Dolomanov et al. 2009). We adopted the scattering factors of Mg^{2+} (Cromer and Mann 1968) and O^{2-} (Tokonami 1965), whereas the F^- and O^{2-} anions are indistinguishable from each other by XRD. For each sample, the structure refinements were conducted in both the single-site and three-site split-atom hydrogen models (e.g. Xu et al. 2013; Chakoumakos et al. 2013), which will be discussed in detail in the following section. For all these three brucite samples, the GooF parameters remain below 1.2, while R_1 for $I > 4\sigma$ and R_{int} are no more than 3.3 % and 5.4 %, respectively.

2.3. *In situ* Raman and FTIR spectra at temperatures

Raman spectra were collected on a Horiba LabRAM HR Evolution system (HORIBA JobinYvon S.A.S., France), with a micro confocal spectrometer and a Nd YAG laser excitation source (P = 20 mW, λ = 532 nm for the second harmonic of the baseline at 1064 nm). Raman shift was firstly calibrated by a silicon single crystal, and datasets were collected in frequency ranges of 50 - 1000 cm^{-1} for the lattice vibrations and 3000 - 4000 cm^{-1} for the OH-stretching modes at room temperature. Next, two sample chips (with diameters of 80 - 90 μm) of $Mg(OH)_{1.78}F_{0.22}$ and $Mg(OH)_{1.16}F_{0.84}$ were loaded on a sapphire window in a Linkam THMS 1500 heating stage, and Raman measurements were conducted from 300 K to 800 K with an interval of 50 K and a heating rate of 10 K/min, and temperatures were controlled by an auto-controlling unit, with an uncertainty typically within 3 K. At each step, the target temperature was firstly maintained for 5 minutes for thermal equilibrium, and then a Raman spectrum (3200 – 4000 cm^{-1}) was recorded in the backscattering direction through a VIS LWD 50× objective with a duration of 5 min and an accumulation of 3 times.

Mid-FTIR measurements were carried out on a Nicolet 5700 FTIR system (Thermofisher, U.S.A.) with a KBr beam-splitter and an MCT-A detector cooled by liquid N_2. The IR-active OH-stretching modes were also recorded in the wavenumber range of 3000 – 4000 cm^{-1}. Two crystal chips from the synthetic F-bearing sample source (with thicknesses of 20 - 30 mm) were loaded at a sapphire window of a custom HS1300G-MK2000 external heating stage (INSTC, U.S.A.). High temperatures were achieved up to 850 K by internal resistant heating with a rate of 15 K/min, and the temperatures were also controlled by an auto controller with an uncertainty within 5 K. At each temperature, FTIR spectra on the sample and background were measured in the transmission mode with an accumulation of 128 scanning times and a resolution of 4 cm^{-1}. Both high-temperature Raman and FTIR spectra were measured in a N_2 protection atmosphere, to avoid potential contamination by CO_2 in the air.

2.4. High-pressure vibrational spectra

Three pairs of diamond anvils with 400-μm culets and very low fluorescence were aligned in shortened symmetric-type diamond anvil cells (DAC) for the high-pressure Raman and FTIR measurements, and we just focused on the internal OH-stretching vibrations above 3000 cm^{-1}. Rhenium gaskets were pre-indented to a thickness about 45 μm with a 290-μm hole drilled at the center. Selected crystals of $Mg(OH)_{1.78}F_{0.22}$, $Mg(OH)_{1.16}F_{0.84}$ and $Mg(OH)_{1.99}F_{0.01}$ (with dimensions approximately 50 × 50 × 20 μm^3) were loaded in the chambers, together with 1 or 2 annealed ruby chips (with diameters less than 5 μm) in each cell. It is noted that Zhu et al. (2019) already carried out high-temperature Raman and FTIR measurements on this natural brucite sample. The pressure transmitting medium, Ar, was cryogenically loaded by cooling from N_2, and the sealed pressures were around 1.5 GPa with the diameters of the holes shrunk by approximately 25 %.

Raman measurements in DACs were conducted up to approximately 20 GPa with a duration of 10 minutes for each spectrum, while mid-FTIR spectra were collected with an accumulation of 256 scans. The pressure gradients inside solid Ar media should be no more than 0.2 GPa in the P-range below 20 GPa at T = 300 K (Klotz et al. 2009), which are smaller than the estimated experimental uncertainties. Pressures were calibrated by the shift of ruby fluorescence line R_1 (Ye et al. 2018) before and after collection of each vibrational spectra, and the R_1 line was measured to be at 694.5 nm at the ambient pressure. The software package of Peakfit v4.12 software was adopted for the analyses of all the Raman and FTIR spectra.

3. Discussion

3.1. Crystal structures

In the brucite structure with trigonal symmetry $P3m1$, the Mg^{2+} cations are coordinated with 6 O^{2-} anions, forming MgO_6 octahedra stacked in layers perpendicular to the *c* axis (e.g. Chakoumakos et al. 1997; Desgranges et al. 1996). The O-H covalent bonds lie between two MgO_6-layers, and interact with three adjacent O-H bonds from the neighboring layer, through O…H attraction as well as H…H repulsion. Consequently, the *c* axis exhibits significantly larger compressibility (Fei and Mao 1993; Catti et al. 1995) and thermal expansivity (Fukui et al. 2003; Xu et al. 2013), as compared with the *a* axis. Both the synthetic F-bearing brucite samples in this study maintained the trigonal structure, and the *a* and *c* axes get shortened with $OH^- = F^-$ substitution, since the radius of F^- (1.33 Å) is slightly smaller than that for O^{2-} (1.40 Å) in 6 coordination (Shannon 1976). The unit-cell volumes of $Mg(OH)_{1.78}F_{0.22}$ and $Mg(OH)_{1.16}F_{0.84}$ are 0.61(9) % and 1.56(8) % smaller, respectively, as compared with that for $Mg(OH)_{1.99}F_{0.01}$.

Two models have been proposed to interpret the hydrogen positions in the crystal structure of brucite (Xu et al. 2013; Chakoumakos et al. 2013). In the single-site model with $x_H = 1/3$ and $y_H = 2/3$, the O-H covalent bond is aligned parallel to the *c* axis. While in the three-site atom-split model, the proton is disordered in three equivalent positions around the threefold rotation axis, with an equal occupancy of 1/3 in each site. To refine the H position in the three-site model, Xu et al. (2013) proposed the constraint of $y_H = 2 \cdot x_H$, which is adopted in this study. Besides, Chakoumakos et al. (2013) alternatively fixed $x_H = 1/3$ and refined both y_H and z_H. Since the occupancies in the hydrogen positions are reduced with the $OH^- = F^-$ substitution, the H occupancies (**Table 3**) are fixed based on the compositions analyzed by EPMA.

The bond lengths and angles (**Table 4**) are calculated using the software package Xtaldraw (Downs et al. 1993)**.** The refined O-H bond lengths are in the range of 1.0 – 1.1 Å for these three brucite samples in both the single-site and three-site models, and the fluorine impact can be ignored considering the resolution of the XRD measurement. However, the averaged O(F)…H distances predicted from the three-site model agree better with those by neutron diffractions (Xu et al. 2013; Chakoumakos et al. 2013), as compared with those from the single-site model which are 0.07 – 0.14 Å shorter. On the other hand, the O(F)…H distance in $Mg(OH)_{1.16}F_{0.84}$ is 0.13(6) Å shorter than that in $Mg(OH)_{1.99}F_{0.01}$ in the three-site model, while the H-O-H angels decrease from 18(3)° in $Mg(OH)_{1.99}F_{0.01}$ to 11(2)° in $Mg(OH)_{1.16}F_{0.84}$ (**Fig. S2** in the supplementary materials). Hence, it is quite possible that the site-split phenomenon and elongation of the O…H distances are caused by neighboring H-H repulsion in the brucite lattice. While $OH^- = F^-$ substitution could alleviate the H-H repulsion in the local structure and make the O…H distances slightly shorter.

In addition, the averaged Mg-O(F) bond lengths become shortened with increasing fluorine concentration, since the radius $r(O^{2-})$ is 0.07 Å larger than $r(F^-)$. The Mg-O(F) bond lengths in $Mg(OH)_{1.78}F_{0.22}$ and $Mg(OH)_{1.16}F_{0.84}$ are 0.0071(13) and 0.0120(14) Å shorter, respectively, than that in the natural sample, while the angles of O(F)-Mg-O(F) and Mg-O(F)-H are almost identical among these samples.

3.2. Fluorine effect on OH-stretching vibrations

The Raman and mid-FTIR spectra at ambient conditions were measured on the two synthetic F-bearing samples, the natural one, as well as the analytical reagent $Mg(OH)_2$ powder for comparison. The fluorine concentration in this purchased sample should be well below 0.1 mol.% since its purity is greater than 99.9 %. Two bands are consistently observed at 285 cm^{-1} (E_g mode) and 450 cm^{-1} (A_{1g} mode) among these four brucite samples with various fluorine concentrations (**Fig. 1a**), while F^- substitution has little effect on the frequencies or intensities of these Raman-active modes. The lattice E_g and A_{1g} modes correspond to the transitional vibrations of OH^- units perpendicular and parallel to the *c* axis, respectively, relative to Mg^{2+} cations at the center of MgO_6-octahedra (e.g. Dowson et al. 1973), which are also sketched in the figure. On the other hand, the internal OH-stretching bands (A_{1g} mode, Raman-active) for $Mg(OH)_{1.78}F_{0.22}$ and $Mg(OH)_{1.16}F_{0.84}$ locate at positions of 4 and 9 cm^{-1} lower than those for the natural and analytical reagent samples (**Fig. 1b**). For the synthetic F-bearing samples, broad 'humps' with very low intensities are detected around the OH-stretching mode, and the hump in $Mg(OH)_{1.16}F_{0.84}$ spreads in a wide range from 3550 to 3700 cm^{-1}. New hydrogen positions will be formed when F^- anions substitute some of OH^- groups in the lattice structures, but the fluorine effect on the OH-stretching vibrations is not clearly reflected in the Raman spectra. Similarly, Hughes and Pawley (2019) synthesized F-bearing humite-group minerals, which are a series of dense hydrous Mg-silicates on the forsterite – brucite joint, and no extra OH-stretching modes were either detected in the Raman spectra, as compared with the OH-pure samples.

Beside the original OH-stretching mode of A_{2u} at 3695 cm^{-1} (denoted as v_2 mode in this FTIR study), additional IR-active vibrations are observed for the synthetic F-bearing samples, such as two strong bands at 3660 (v_3) and 3644 (v_4) cm^{-1} and two weak and relatively broader modes at 3804 (v_1) and 3513 (v_5) cm^{-1} (**Fig. 1c**). For the sample of $Mg(OH)_{1.16}F_{0.84}$, the intensities of v_3 and v_4 are even larger than that for v_2. The v_1 band at the highest wavenumber (frequency) should be associated with the F…H interaction, which is stronger than the O…H attraction, since the negativity of fluorine is even larger than that for oxygen (James and Lord 1992). While the vibrations at lower wavenumbers (v_3, v_4 and v_5) are attributed to new O…H interactions induced by F-substitution.

We propose a correlation between the IR-active OH-stretching bands (v_2, v_3, v_4 and v_5) and the F substitution in the local structures in **Fig. 2(a-d)**. In the brucite structure, each O^{2-} anion is coordinated with 1 H^+ and 3 Mg^{2+} cations, as shared by three neighboring MgO_6 octahedra. The v_3, v_4 and v_5 modes, in the order of decreasing wavenumber, corresponds to the cases that 1, 2 and 3 OH^- neighboring groups are substituted by F^- anions, respectively. If the neighboring OH^- group is substituted by F^-, the adjacent H-H repulsion effect will be alleviated, which could decrease the O…H distances and the splitting H-O-H angle. In addition, it has also been observed that the $OH^- = F^-$ substitution induces extra OH-stretching modes at lower wavenumbers in the FTIR spectra of humite-group minerals due to the alleviation of neighboring H-H repulsion (e.g. Lin et al. 1999, 2000; Mernagh et al. 1999; Liu et al. 2019, 2021).

3.3. OH-stretching modes at high temperature

In situ high-temperature Raman and FTIR spectra of the synthetic F-bearing brucite samples are present in **Fig. 3(a-d)**. The intensities of the OH-stretching bands measured when quenched from 750 K, remain almost the same as those before heating. The peaks of the IR-active vibrations completely vanish at T = 800 K for $Mg(OH)_{1.78}F_{0.22}$ while at 850 K for $Mg(OH)_{1.16}F_{0.84}$. While the previous studies reported a dehydration point around 700 K for the F-free samples (Fuji-Ta et al. 2007; Liu et al. 2018; Zhu et al. 2019), which is 100 – 150 K lower than those for the F-bearing ones in this study. The frequencies of the OH-stretching modes are plotted as a function of temperature for both the synthetic F-bearing sample in **Fig. 4(a-b)**, and a comparison is made with the high-T vibrational spectra of the natural sample from Zhu et al. (2019). The weak and broad v_1 band for the F…H interaction could not be resolved above 700 K for $Mg(OH)_{1.16}F_{0.84}$, and the strong v_3 and v_4 peaks cannot be distinguished from each other at $T = 700$ K for $Mg(OH)_{1.78}F_{0.22}$, since the IR signals typically become weaker and broader at elevated temperature. The proton positions become disordered with increasing temperature, and correspondingly the distribution of O-H distances gets broadened for each OH-stretching mode. Nevertheless, these vibrational bands were separated again from each other when quenched to room temperature (**Fig. 3c** and **3d**).

Linear regressions are fitted for these modes at high temperatures, and the derived slopes ($(\partial v_i/\partial T)_P$, in the unit of $cm^{-1}\cdot K^{-1}$) are listed in **Table S2** in the supplementary materials. All the OH-stretching modes shift to lower frequencies with increasing temperature, except for the v_5 bands around 3510 cm^{-1}. According to the previous studies on hydrogen bonds (Libowitzky 1999; Mockenhaupt et al. 1998), the critical O…H distance ($d_{O\ldots H}$) for the presence of hydrogen bonds is 2.4 Å in the brucite-type minerals, which corresponds to a OH-stretching vibration below 3600 cm^{-1}. Hence, hydrogen bonds could only be formed for the v_5 band at the lowest wavenumber. In the absence of forming hydrogen bond, the frequencies of the v_2, v_3 and v_4 modes are in negative correlation of the adjacent Mg-O bond length (Beckenkamp and Lutz 1992; Lutz 1995), and consequently, the expansion of Mg-O bond would yield 'red-shift' for these vibrations at high temperatures. On the other hand, the 'blue-shift' of v_5 modes at elevated temperature could be explained by the expansion of the corresponding hydrogen bond length. The value of $(\partial v_i/\partial T)_P$ is generally in negative dependence with the frequency (in cm^{-1}) for the v_2, v_3, v_4 and v_5 modes from 3500 to 3700 cm^{-1} (**Fig. 5**). Fluorine is smaller with larger electronegativity, as compared with oxygen. In this case, F-substitution in a MgO_6 octahedron could form shorter (stronger) Mg-F bond, and weaken the strength of the adjacent Mg-O bonds, which would further become less sensitive to variation of temperature. Hence, the frequencies of the v_3 and v_4 modes decrease at smaller rates with increasing temperature, as compared with that for v_2.

To further test the fluorine effect on the high-temperature stability of brucite, we loaded a $Mg(OH)_{1.78}F_{0.22}$ chip (in a dimension of 50 × 50 × 20 μm^3) in the heating stage for FTIR measurement. Next, the temperature was maintained at 750 K for up to 12 hours, and the chamber was filled with a N_2 atmosphere to protect the sample from CO_2 in the air. At the heating intervals of 2, 5, 8 and 12 hours, the sample was quenched to room temperature, and FTIR spectra were recorded from 3400 to 3900 cm^{-1} (**Fig. S3(a,b)** in the supplementary materials). The integration of these OH-stretching bands remains almost the same, suggesting no dehydration throughout the heating procedure as long as 12 hours. On the other hand, dehydration in the F-free brucite samples was observed to complete in a duration well within 1 hour, at the temperature around 700 K and P = 0 GPa (Liu et al. 2018; Zhu et al. 2019). Hence, the dehydration points in these F-bearing brucite samples are 100 – 150 K higher than those for $Mg(OH)_2$ even at ambient pressure.

3.4. Pressure dependence of OH-stretching modes

Representative high-pressure Raman and FTIR spectra (3300–3900 cm^{-1}) are shown in **Fig. 6(a–f)** for the two synthetic and one natural samples. A new weak band appears around 3670 cm^{-1} at P = 8.4 GPa in the Raman spectrum for $Mg(OH)_{1.16}F_{0.84}$ (**Fig. 6b**), and then shifts to lower frequency at higher pressure. A new hydrogen position is induced maybe by the high-P phase transition in this sample with 42 mol.% F, and further investigation is needed for confirmation. Nevertheless, this Raman-active band is not detected in the other two brucite samples with lower fluorine concentrations. Besides, the OH-stretching bands systematically got broader with increasing pressure, and the 'triplet' for IR-active ν_2, ν_3 and ν_4 bands becomes a broad 'hump' for the synthetic samples (from 3550 to 3570 cm^{-1}) around 15 – 16 GPa (**Fig. 6(d,e)**). Kruger et al. (1989) also observed that the full width at half-maximum (FWHM) of the IR-active OH-stretching bands increase at elevated pressure in both $Mg(OH)_2$ and $Ca(OH)_2$, and attributed it to the anharmonicity caused by the enhanced hydrogen bonding during compression. Besides, a previous high-pressure Raman measurement on brucite (Duffy et al. 1995) indicated that the OH-stretching mode gets broadened at a larger rate with pressure in neon medium (under quasi-hydrostatic condition), as compared with that measured without pressure medium. They suggested that nonhydrostatic pressure distribution could also have some contribution to the broadening of the peak, together with the intrinsic effect.

An additional absorption peak emerges around 3640 cm^{-1} at 4.5 GPa in the FTIR spectrum for the natural brucite (**Fig. 6f**), which becomes significantly stronger than the original one around 3690 cm^{-1} and shifts to lower wavenumber at elevated pressure. Similar phenomena were also observed in another natural brucite sample at P = 2.9 GPa (300 K) in a pressure medium of fluocarbon fluid (Shinoda and Aikawa 1998) or KBr (Shinoda et al. 2002). This pressure-induced mode was attributed to the formation of a secondary OH dipole by proton transferring between donor OH^- group and acceptor O^{2-} between two adjacent layers, and such one-proton-state to two-proton-state transition is reversible at high-P,T conditions (Shinoda et al. 2002). On the other hand, Kruger et al. (1989) conducted the high-pressure measurement on a reagent $Mg(OH)_2$ sample, and they observed a weak peak around 3650 cm^{-1} (hot band) when compressed to a pressure as high as 9.3 GPa. This new peak was still detectable when decompressed to 4.4 GPa, as indicated in their Fig. 2. Nevertheless, it is reasonable to associate that hot band to a transition from the 1st excited IR-active state (A_{2u}, n = 1) to the second overtone ($A_{2u} \times A_{2u}$, n = 2), since its intensity is much lower as compared with the (original) fundamental one. Hence, we speculate that impurities or vacancies in naturally-occurring brucite are essential for the formation of pressure-induced OH dipoles with high intensities. It should also be noted that the frequency of this new proton state is very close to the v_4 modes in the F-bearing sample, and both compression and F-substitution could have a similar effect on creating new H positions in the lattice.

Variation of the OH-stretching modes with pressure is presented in **Fig. 7(a-c)** for each brucite sample, and linear regressions are fitted for the vibrational bands with the slopes ($(\partial v_i/\partial P)_T$, $cm^{-1}\cdot GPa^{-1}$) listed in **Table S3** in the supplementary materials. Most bands shift to lower frequencies at elevated pressure, except the v_2 modes in the synthetic samples (at the rates of 2.2 ~ 2.5 cm^{-1}/GPa, around 3690 cm^{-1}). Besides, the Raman-active and IR-active OH-stretching modes in $Mg(OH)_{1.99}F_{0.01}$ decrease at the rates of -7.0 and -0.6 cm^{-1}/K, respectively, which are in general agreement with the previous experiments (Duffy et al. 1995; Kruger et al. 1989). Since the c axis exhibits significantly larger compressibility than the a-axis in brucite, the interlayer O…H distances become shorter rapidly at elevated pressures (e.g. Parise et al. 1994; Catti et al. 1995). The DFT calculation (Mookherjee and Stixrude 2006) also supported that the O…H bond gets shortened while the covalent O-H bond remains almost the same in the P-range at least to 30 GPa. Consequently, hydrogen bonds are readily formed and enhanced for most of the protons (H^+) in the brucite samples, and the frequencies of the OH-stretching bands are basically in positive correlation with the O…H bond lengths (e.g. Libowitzky 1999; Nakamoto et al. 1955). In addition, both the IR-active and Raman-active OH-stretching modes in the normal brucite samples were observed to show 'blue-shift' during decompression (Kruger et al. 1989; Duffy et al. 1995). Hence, variation of the hydrogen bonds is essentially reversible at high-pressure conditions. The IR-active v_1 peaks (around 3800 cm^{-1}) could only be resolved up to 6 GPa, and they decrease at the rates of -4.9 ~ -5.8 cm^{-1}/GPa, suggesting that the F…H hydrogen bonds could also be strengthened at high pressures.

The pressure dependence of the OH-stretching modes, $(\partial v_i/\partial P)_T$, is typically in positive correlation with the vibrational frequency in the range from 3500 to 3700 cm^{-1} (**Fig. 8**), as opposed to the relationship between $(\partial v_i/\partial T)_P$ and v_i at high temperatures. As compared with the longer O…H bands, the shorter ones (at lower wavenumbers) get compressed more quickly at elevated pressure, since their negative slopes of $(\partial v_i/\partial P)_T$ are in larger magnitudes. The $OH^- = F^-$ substitution alleviates the adjacent H-H repulsion in local structures, which further expedites the compression of the O…H bond in hydrous minerals (e.g. Liu et al. 2019, 2021).

4. Mineral physical and geochemical implications

Fluorine substitution ($OH^- = F^-$) is widely observed in hydrous minerals, such as the serpentine-group, mica and humite-group minerals (e.g. Smith et al. 1981; Ottolini et al. 2000), since the radii of F^- and O^{2-} are quite similar to each other (Shannon 1976). The incorporated F^- anions can alleviate neighboring H-H repulsion in the local structures of these hydrous phases, and strengthen (shorten) the corresponding hydrogen bonds, making the lattice structures more stable. Consequently, the *P-T* stability fields of hydrous minerals are significantly expanded due to the F^- effect. For example, fluorine stabilizes clinohumite to much higher temperatures, well above the geotherm in the subduction slab (Engi and Lindsley 1980; Grützner et al. 2017). In this study, we observed that the dehydration points of the synthetic F-bearing brucite samples are 800 – 850 K at the ambient pressure, which is 100 – 150 K higher than that for F-free samples in the atmosphere (Liu et al. 2018; Zhu et al. 2019). In the presence of fluorine, brucite could also be stable at higher *P-T* conditions in subduction zones. Besides, it also deserves investigations on fluorine substitution in the dense hydrous Mg-silicates (DHMSs), such as phase A, supper hydrous phase B, phase E as well as phase D, which will provide us new insight into hydrogen and fluorine cycling in the subduction slabs, as well as in the mantle transition zone (410 – 660 km depth) and lower mantle (below 660 km depth).

The crystal structure refinements on the F-bearing brucite samples indicate that F^- incorporation shrinks the unit-cell volumes as well as the averaged Mg-O(F) bond length. Previous measurements on equations of state (EOSs) support that fluorine incorporation significantly increases the isothermal bulk moduli for topaz (e.g. Gatta et al. 2006, 2014) and humite-group minerals (e.g. Friedrich et al. 2002; Kuribayashi et al. 2004). Hence, further studies are needed for the fluorine effect on the thermoelastic properties (including *P-V-T* EOSs) for DHMS phases at high *P-T* conditions in the deep Earth interior. According to the high-pressure FTIR measurements, the shortened O…H bonds in brucite (at lower frequencies) are more compressible (shifting to lower frequencies at larger rates with increasing pressure), as compared with the original O…H bonds at higher wavenumbers. Thompson et al. (2016) also proposed that the low-frequency OH-stretching bands in amphiboles would get softened and are more likely to participate in hydrogen bond symmetrization at elevated pressures. It is quite possible that fluorine substitution could contribute to hydrogen bond symmetrization in hydrous minerals at high pressures.

On the other hand, fluorine substitution should also have a pronounced impact on the equilibrium hydrogen isotope fractionation between hydrous minerals and fluids. Theoretical calculations indicate that the reduced partition function ratio (β factor) in hydrous minerals (like brucite) is dominantly determined by the OH-stretching modes at high frequencies (e.g. Reynard and Caracas 2009). While F^- incorporation generates new O…H bonds at lower energies (frequencies), which makes the lattice structures more stable. Consequently, the β factors for hydrous minerals would become smaller, and the heavier deuterium atoms would be less likely to fractionate into the hydrous mineral phases. This result provides us a useful clue to study equilibrium D/H fractionation between hydrous minerals and water in the presence of fluorine.

Acknowledgment: This study was supported by the National Key Research and Development Program of China (Grant No. 2018YFA0702700), the National Natural Science Foundation of China (Grant No. 42072050), and the Science Fund for Distinguished Young Scholars of Hubei Province (2020CFA104). The multi-anvil press synthesis, Raman and FTIR measurements were conducted at China University of

Geosciences (Wuhan), the single-crystal XRD experiments were carried at Huazhong University of Science and Technology, and EPMA analyses were carried out at Second Institute of Oceanography, MNR. Many thanks to Dr. Jihao Zhu and Dr. Yan Qin for their experimental assistances.

Reference:

Beckenkamp, K., and Lutz, H.D. (1992) Lattice vibration spectra Part LXXII. OH stretching frequencies of solid hydroxides—Correlation with structural and bonding data. Journal of Molecular Structure, 270, 393–405.

Catti, M., Ferraris, G., Hull, S., and Pavese, A. (1995) Static compression and H disorder in, Mg $(OH)_2$, to 11 GPa: A powder neutron diffraction study. Physics and Chemistry of Minerals, 22(3), 200–206.

Chakoumakos, B.C., Loong, C.K., and Schultz, A.J. (1997) Low-temperature structure and dynamics of brucite. Journal of Physical Chemistry B, 101(46), 9458–9462.

Chakoumakos, B.C., Horita, J., and Garlea, V.O. (2013) H/D isotope effects in brucite at low temperatures. American Mineralogist, 98(1), 1-6.

Cromer, D.T., and Mann, J. (1968) X-ray scattering factors computed from numerical Hartree-Fock wave functions. Acta Crystallographica, A24, 321–325.

Dawson, P., Hadfield, C.D., and Wilkinson, G.R. (1973) The polarized infra-red and Raman spectra of $Mg(OH)_2$ and $Ca(OH)_2$. Journal of Physics and Chemistry of Solids, 34(7), 1217-1225.

Desgranges, L., Calvarin, G., and Chevrier, G. (1996) Interlayer interactions in M $(OH)_2$: A neutron diffraction study of Mg $(OH)_2$. Acta Crystallographica, 52(1), 82–86.

Dolomanov, O.V., Bourhis, L.J., Gildea, R.J, Howard, J.A.K., and Puschmann, H. (2009) OLEX2: a complete structure solution, refinement and analysis program. Journal of Applied Crystallography, 42(2), 339-341.

Downs, R.T., Bartelmehs, K.L., Gibbs, G.V., and Boisen, M.B. (1993) Interactive software for calculating and displaying X-ray or neutron powder diffractometer patterns of crystalline materials. American Mineralogist, 78(9-10), 1104-1107.

Duffy, T.S., Meade, C., Fei, Y., Mao, H.K., and Hemley, R.J. (1995) High-pressure phase transition in brucite, Mg $(OH)_2$ American Mineralogist, 80(3-4), 222-230.

Engi, M., and Lindsley, D.H. (1980) Stability of titanian clinohumite: experiments and thermodynamic analysis. Contributions to Mineralogy and Petrology, 72, 1935-1938.

Fei, Y., and Mao, H.K. (1993) Static compression of Mg $(OH)_2$ to 78 GPa at high temperature and constraints on the equation of state of fluid H_2O. Journal of Geophysical Research, 98(B7), 11, 875–11,884.

Friedrich, A., Lager, G.A., Ulmer, P., Kunz, M., and Marshall, W.G. (2002) High-pressure single-crystal X-ray and powder neutron study of F, OH/OD-chondrodite: compressibility, structure, and hydrogen bonding. American Mineralogist, 87, 931-939.

Fuji-Ta, K., Katsura, T., Matsuzaki, T., and Ichiki, M. (2007) Electrical conductivity measurements of brucite under crustal pressure and temperature conditions. Earth, Planets and Space, 59(6), 645–648.

Fukui, H., Ohtaka, O., Suzuki, T., and Funakoshi, K. (2003) Thermal expansion of Mg $(OH)_2$ brucite under high pressure and pressure dependence of entropy. Physics and Chemistry of Minerals, 30(9), 511–516.

Gatta, G.D., Nestola, F., and Ballaran, T.B. (2006) Elastic behavior and structural evolution of topaz at high pressure. Physics and Chemistry of Minerals, 33(4), 235-242.

Gatta, G.D., Morgenroth, W., Dera, P., Petitgirard, S., and Liermann, H.P. (2014) Elastic behavior and pressure-induced structure evolution of topaz up to 45 GPa. Physics and Chemistry of Minerals, 41(8), 569-577.

Grützner, T., Klemme, S., Rohrbach, A., Gervasoni, F., and Berndt, J. (2017) The role of F-clinohumite in volatile recycling processes in subduction zones. Geology, 45(5), 443-446.

Horita, J., Cole, D.R., Polyakov, V.B., and Driesner, T. (2002) Experimental and theoretical study of pressure effects on hydrogen isotope fractionation in the system brucite-water at elevated temperatures. Geochimica et Cosmochimica Acta, 66(21), 3769–3788.

Horita, J., dos Santos, A.M., Tulk, C.A., Chakoumakos, B.C., and Polyakov, V. B. (2010) High-pressure neutron diffraction study on H–D isotope effects in brucite. Physics and Chemistry of Minerals, 37(10), 741–749.

Horita, J., Driesner, T., and Cole, D.R. (2018) Hydrogen isotope fractionation in the system brucite-water ± NaCl to elevated temperatures and pressures: Implications for the isotopic property of NaCl fluids under geologic conditions. Geochimica et Cosmochimica Acta, 235, 140–152.

Hughes, L. and Pawley, A. (2019) Fluorine partitioning between humite-group minerals and aqueous fluids: implications for volatile storage in the upper mantle. Contributions to Mineralogy and Petrology, 174, 78.

James, A.M. and Loard, M.P. (1992) MacMillan's chemical and physical data. Macmillan Press, Basingstoke.

Jiang, F., Speziale, S., and Duffy, T.S. (2006) Single-crystal elasticity of brucite, $Mg(OH)_2$, to 15 GPa by Brillouin scattering. American Mineralogist, 91, 1893-1900.

Kanzaki, M. (1991) Dehydration of brucite ($Mg\ (OH)_2$) at high pressures detected by differential thermal analysis. Geophysical Research Letters, 18(12), 2189–2192.

Kieffer, S.W. (1979) Thermodynamics and lattice vibrations of minerals: 3. Lattice dynamics and an approximation for minerals with application to simple substances and framework silicates. Reviews of Geophysics, 17(1), 35–59.

Klotz, S., Chervin, J.-C., Munsch, P., and Le Marchand, G. (2009) Hydrostatic limits of 11 pressure transmitting media. Journal of Physics D: Applied Physics, 42, 075413.

Kruger, M.B., Williams, Q., and Jeanloz, R. (1989) Vibrational spectra of $Mg\ (OH)_2$ and $Ca\ (OH)_2$ under pressure. The Journal of Chemical Physics, 91(10), 5910-5915.

Kuribayashi, T., Kagi, H., Tanaka, M., Akizuki, M., and Kudoh, Y. (2004) High-pressure single-crystal X-ray diffraction and FT-IR observation of natural chondrodite and synthetic OH-chondrodite. Journal of Mineralogical and Petrological Sciences, 99(3), 118-129.

Libowitzky, E. (1999) Correlation of O-H stretching frequencies and O-H … O hydrogen bond lengths in minerals. Monatshefte für Chemie, 130(8), 1047–1059.

Lin, C.C., Liu, L.G., and Irifune, T. (1999) High-pressure Raman spectroscopic study of chondrodite. Physics and Chemistry of Minerals, 26(3), 226-233.

Lin, C.C., Liu, L.G., Mernagh, T.P., and Irifune, T. (2000) Raman spectroscopic study of hydroxyl-clinohumite at various pressures and temperatures. Physics and Chemistry of Minerals, 27(5), 320-331.

Liu, C.J., Zhang, R.X., Shen, K.W., Liu, T., Wen, W., and Wang, D.J. (2018) An in situ kinetic study of the dehydration of brucite using synchrotron X-ray powder diffraction. Canadian Mineralogist, 56(1), 101–108.

Liu, D., Pang, Y., Ye, Y., Jin, Z., Smyth, J.R., Yang, Y., and Wang, Z. (2019) In-situ high-temperature vibrational spectra for synthetic and natural clinohumite: Implications for dense hydrous magnesium silicates in subduction zones. American Mineralogist, 104(1), 53-63.

Liu, D., Smyth, J.R., Zhu, X., Miao, Y., Hu, Y., Chen, G., and Ye, Y. (2021) High-pressure vibrational spectra of humite-group minerals: Fluorine effect on thermodynamic properties and hydrogen bonds. Physics of the Earth and Planetary Interiors, 312, 106654.

Lutz, H.D. (1995) Hydroxide ions in condensed materials—Correlation of spectroscopic and structural data. In Coordination Chemistry. Structure and Bonding (Vol. 82, pp. 85–103). Berlin, Heidelberg: Springer.

Ma, M., Liu, W., Chen, Z., Liu, Z., and Li, B. (2013) Compression and structure of brucite to 31 GPa from synchrotron X-ray diffraction and infrared spectroscopy studies. American Mineralogist, 98(1), 33-40.

McDonough, W.F. and Sun, S. (1995) The composition of the Earth. Chemical Geology, 120, 223-253.

Méheut, M., Lazzeri, M., Balan, E., and Mauri, F. (2007) Equilibrium isotopic fractionation in the kaolinite, quartz, water system: Prediction from first-principles density-functional theory. Geochimica et Cosmochimica Acta, 71(13), 3170–3181.

Méheut, M., Lazzeri, M., Balan, E., and Mauri, F. (2010) First-principles calculation of H/D isotopic fractionation between hydrous minerals and water. Geochimica et Cosmochimica Acta, 74(14), 3874–3882.

Mernagh, T.P., Liu, L. G., and Lin, C.C. (1999) Raman spectra of chondrodite at various temperatures. Journal of Raman Spectroscopy, 30(10), 963-969.

Miao, Y.F., Pang, Y.W., Ye, Y., Smyth, J.R., Zhang, J.F., Liu, D., Wang. X., and Zhu, X. (2019) Crystal Structures and High Temperature Vibrational Spectra for Synthetic Boron and Aluminum Doped Hydrous Coesite. Crystals, 9(12), 642.

Mitra, S.S. (1962) Vibration spectra of solids. In F. Seitz, and D. Turnbull (Eds.), Solid state physics (pp. 1–

80). New York: Academic.

Mockenhaupt, C., Zeiske, T., and Lutz, H.D. (1998) Crystal structure of brucite-type cobalt hydroxide β-Co{O(H,D)}$_2$—Neutron diffraction, IR and Raman spectroscopy. Journal of Molecular Structure, 443(1-3), 191–196.

Mookherjee, M. and Stixrude, L. (2006) High-pressure proton disorder in brucite. American Mineralogist, 91, 127-134.

Nakamoto, K., Margoshes, M., and Rundle, R.E. (1955) Stretching frequencies as a function of distances in hydrogen bonds. Journal of the American Chemical Society, 77(24), 6480-6486.

Ottolini, L., Cámara, F., and Bigi, S. (2000) An investigation of matrix effects in the analysis of fluorine in humite-group minerals by EMPA, SIMS, and SREF. American Mieneralogist, 85(1), 89-102.

Pagé, L. and Hattori, K. (2019) Abyssal serpentinites: Transporting halogens from Earth's surface to the deep mantle. Minerals, 9, 61.

Parise, J.B., Leinenweber, K., Weidner, D.J., Tan, K., and Dreele, R.B.V. (1994) Pressure-induced H bonding: Neutron diffraction study of brucite, Mg (OD)$_2$, to 9.3GPa. American Mineralogist, 79, 193–196.

Reynard, B., and Caracas, R. (2009) D/H isotopic fractionation between brucite Mg (OH)$_2$ and water from first-principles vibrational modeling. Chemical Geology, 262(3-4), 159–168.

Saccocia, P.J., Seewald, J.S., and Shanks, W.C. (1998) Hydrogen and oxygen isotope fraction between brucite and aqueous NaCl solutions from 250 to 450 degrees C. Geochimica et Cosmochimica Acta, 62(3), 485–492.

Satake, H., and Matsuo, S. (1984) Hydrogen isotopic fractionation factor between brucite and water in the temperature-range from 100- degrees-C to 510-degrees-C. Contributions to Mineralogy and Petrology, 86(1), 19–24.

Shannon, R.D. (1976) Revised effective ionic radii and systematic studies of interatomic distances in halides and chalcogenides. Acta Crystallographica, A32, 751-767.

Sheldrick, G.M. (2015) Crystal structure refinement with SHELEL. Acta Crystallographica , 71(1), 3-8.

Shinoda, K., and Aikawa, N. (1998) Interlayer proton transfer in brucite under pressure by polarized IR spectroscopy to 5.3 GPa. Physics and Chemistry of Minerals, 25(3), 197–202.

Shinoda, K., Yamakata, M., Nanba, T., Kimura, H., Moriwaki, T., Kondo, Y., and Aikawa, N. (2002) High-pressure phase transition and behavior of protons in brucite $Mg(OH)_2$: a high-pressure–temperature study using IR synchrotron radiation. Physics and Chemistry of Minerals, 29(6), 396-402.

Smith, J.V., Delaney, J.S., Hervig, R.L., and Dawson, J.B. (1981) Storage of F and Cl in the upper mantle: geochemical implications. Lithos, 14, 133-147.

Straub, S.M. and Layne, G.D. (2003) The systematics of chlorine, fluorine, and water in Izu arc front volcanic rocks: Implications for volatile recycling in subduction zones. Geochimica et Cosmochimica Acta, 67, 4179-4203.

Thompson, E.C., Campbell, A.J., and Liu, Z. (2016) In-situ infrared spectroscopic studies of hydroxyl in amphiboles at high pressure. American Mineralogist, 101(3), 706-712.

Tokonami, M. (1965) Atomic scattering factor for O^{2-}.Acta Crystallographica, 19, 486.

Wang, X., Xu, X., Ye, Y., Wang, C., Liu, D., Shi, X., Wang, S., and Zhu, X. (2019) In-situ high-temperature XRD and FTIR for calcite, dolomite and magnesite: Anharmonic contribution to the thermodynamic properties. Journal of Earth Science, 30, 964–976.

Wang, S., Zhang, J. H., Smyth, J.R., Zhang, J.F., Liu, D., Zhu, X., Wang. X., and Ye, Y. (2020) Crystal structure, thermal expansivity and high-temperature vibrational spectra on natural hydrous rutile. Journal of Earth Science, 31(6), 1190-1199.

Wunder, B. (1998) Equilibrium experiments in the system $MgO–SiO_2–H_2O$ (MSH): stability fields of clinohumite-OH [$Mg_9Si_4O_{16}(OH)_2$], chondrodite-OH [$Mg_5Si_2O_8(OH)_2$] and phase A ($Mg_7Si_2O_8(OH)_6$). Contributions to Mineralogy and Petrology, 132(2), 111–120.

Xia, X., Weidner, D.J., and Zhao, H. (1998) Equation of state of brucite: single-crystal Brillouin spectroscopy study and polycrystalline pressure-volume-temperature measurements. American Mineralogist, 83, 68-74.

Xu, B., and Zheng, Y.F. (1998) Experimental studies of oxygen and hydrogen isotope fractionations between precipitated brucite and water at low temperatures. Geochimica et Cosmochimica Acta, 63(13-14), 2009-2018.

Xu, H., Zhao, Y., Vogel, S.C., Daemen, L.L., and Hickmott, D.D. (2007a) Anisotropic thermal expansion and hydrogen bonding behavior of portlandite: A high-temperature neutron diffraction study. Journal of Solid State Chemistry, 180, 1519-1525.

Xu, H., Zhao, Y., Zhang, J., Hickmott, D.D., and Daemen, L.L. (2007b) In situ neutron diffraction study of deuterated portlandite $Ca(OD)_2$ at high pressure and temperature. Physics and Chemistry of Minerals, 34, 223-232.

Xu, H., Zhao, Y., Hickmott, D.D., Lane, N.J., Vogel, S.C., Zhang, J., and Daemen, L.L. (2013) High temperature neutron study of deuterated brucite. Physics and Chemistry of Minerals, 40(10), 799–810.

Ye, Y., Brown, D.A., Smyth, J.R., Panero, W.R., Jacobsen, S.D., Chang, Y.Y., Townsend, J.P., Thomas, S.M., Hauri, E.H., Dera, P., and Frost, D.J. (2012) Compressibility and thermal expansion of hydrous ringwoodite with 2.5(3) wt% H_2O. American Mineralogist, 97 (4), 573–582.

Ye, Y., Shim, S., Prakapenka, V., and Meng, Y. (2018) Equation of state of solid Ne intercalibrated with the MgO, Au, Pt, NaCl-B2, and ruby pressure scales up to 130 GPa. High Pressure Research, 38, 377–395.

Zhu, X., Guo, X., Smyth, J.R., Ye, Y., Wang, X., and Liu, D. (2019) High-temperature vibrational spectra between Mg $(OH)_2$ and Mg $(OD)_2$: Anharmonic contribution to thermodynamics and D/H fractionation for brucite. Journal of Geophysical Research: Solid Earth, 124(8), 8267-8280.

Figure captions:

Fig. 1 The Raman spectra and IR spectra measured at the ambient condition for the **(a)** lattice vibrations, **(b)** Raman-active and **(c)** IR-active OH-stretching modes in the brucite samples with various F concentrations. The backgrounds have been subtracted for the FTIR spectra and hereafter in the following figures, and the fitted peak positions are labelled in the figures. The lattice and OH internal vibrations are also sketched above the measured bands, and the *c* axis is along the vertical direction in the plane.

Fig. 2(a-d) Sketches for the correlation between the measured IR-active OH-stretching bands and the fluorine substitution in the local crystal structures, which are viewed along the *c* direction. Only the F^- and O^{2-} anions on the upper side of the MgO_6 layer are shown as large balls, and the protons (small balls) are connected to O^{2-} according to the three-site split model. The Mg^{2+} cations are shown as medium balls at the centers of the octahedra, and the target OH^- groups are marked inside circles.

Fig. 3 Selected *in situ* high-temperature Raman **(a,b)** and FTIR spectra **(c,d)** for the OH-stretching bands in $Mg(OH)_{1.78}F_{0.22}$ **(a,c)** and $Mg(OH)_{1.16}F_{0.84}$ **(b,d)**. The quenched vibrational spectra after heating are also compared in the figures.

Fig. 4 The Raman-active (five-stars) and IR-active (circles) OH-stretching modes as a function of temperature for $Mg(OH)_{1.78}F_{0.22}$ **(a)** and $Mg(OH)_{1.16}F_{0.84}$ **(b)**.

Fig. 5 Summary for the temperature dependence of the OH-stretching bands. $Mg(OH)_{1.99}F_{0.01}$ is from Zhu et al. (2019), while $Mg(OH)_{1.78}F_{0.22}$ and $Mg(OH)_{1.16}F_{0.84}$ are from this study.

Fig. 6 Representative high-pressure Raman **(a,b,c)** and FTIR **(d,e,f)** spectra (3400 – 3900 cm^{-1}) of $Mg(OH)_{1.78}F_{0.22}$ **(a,d)**, $Mg(OH)_{1.16}F_{0.84}$ **(b,e)** and $Mg(OH)_{1.99}F_{0.01}$ **(c,f)**.

Fig. 7 Variations of the OH-stretching modes with pressure for $Mg(OH)_{1.78}F_{0.22}$ **(a)**, $Mg(OH)_{1.16}F_{0.84}$ **(b)** and $Mg(OH)_{1.99}F_{0.01}$ **(c)**.

Fig. 8 Comparison of the pressure dependences for the OH-stretching modes in the synthetic and natural brucite samples from this study.

Table 1. Electron-microprobe analyses for synthetic and natural brucite samples

	R1201	R1202	Natural
$MgO^{@}$ (wt%)	68.1(4)	66.6(5)	68.7(5)
F^- (wt%)	6.92(5)	26.46(4)	0.44(6)
H_2O^* (wt%)	27.17	17.20	30.51
$Total^{\#}$ (wt.%)	99.3(5)	99.1(5)	99.5(6)
Mg (*apfu*)	1.000(7)	1.000(8)	1.000(8)
F	0.216(2)	0.844(1)	0.014(1)
OH	1.784	1.156	1.986

@: The weight percentage corresponds to the sum of MgO and MgF_2 with the conversion of MgF_2 = MgO.

*: Calculated from the stoichiometry of $Mg(OH)_{2-x}F_x$, and the molar ratio of $n(Mg^{2+}) : [n(F^-) + 2 \cdot n(H_2O)]$ is assumed to be 1 : 2.

#: The total weight percentage is equal to $w(MgO) + w(H_2O) + w(F^-) \cdot [1 - m_O/(2 \cdot m_F)]$, where m_O and m_F are the atomic weights for oxygen and fluorine, respectively.

Table 2. Unit-cell parameters and intensity data collection parameters at the ambient condition.

	$Mg(OH)_{1.78}F_{0.22}$	$Mg(OH)_{1.16}F_{0.84}$	$Mg(OH)_{1.99}F_{0.01}$
*a (*Å)	3.1426(8)	3.1318(4)	3.1507(11)
c (Å)	4.7758(16)	4.7628(13)	4.780(2)
V ($Å^3$)	40.85(2)	40.456(15)	41.10(3)
No. total reflections	413	361	188
No. unique total refl.	65	63	59
No. unique refl. with $I > 4\sigma$	57	47	57
Goof (single-site)	1.151	1.080	1.065
(split-site)	1.139	1.086	1.044
R_1 for all (%) (single-site)	3.98	5.55	2.08
(split-site)	3.99	5.53	2.10
R_1 for $I > 4\sigma$ (%) (single-site)	3.68	2.86	2.05
(split-site)	3.70	2.84	2.08
R_{int} (%) (single-site)	4.65	5.40	1.44
(split-site)	4.65	5.40	1.44

$Mg(OH)_{1.78}F_{0.22}$ $Mg(OH)_{1.16}F_{0.84}$ $Mg(OH)_{1.99}F_{0.01}$

single-site hydrogen model				
O(F)[$]	*z*	0.2171(3)	0.2179(4)	0.2182(2)
H[@]	*z*	0.425*	0.44(2)	0.425(9)
	ocpy[&]	0.892	0.578	0.993
three-site split-atom hydrogen model				
O(F)[$]	*z*	0.2171(3)	0.2180(4)	0.2182(2)
H[#]	*x*	0.39*	0.37(5)	0.39(1)
	y	0.78*	0.74(10)	0.78(2)
	z	0.424*	0.442(19)	0.424(7)
	ocpy[&]	0.297	0.193	0.331

Table 3. The refined atomic coordinates in both the single-site and three-site split-atom hydrogen models.

[$]: $x_{\mathrm{O}} = 1/3$, $y_{\mathrm{O}} = 2/3$, while $x_{\mathrm{Mg}} = y_{\mathrm{Mg}} = z_{\mathrm{Mg}} = 0$ in both the single-site and three-site model.

[@]: $x_{\mathrm{H}} = 1/3$ and $y_{\mathrm{H}} = 2/3$ in the single-site model.

[#]: The atomic coordinate for H is constrained as $y_{\mathrm{H}} = 2x_{\mathrm{H}}$ in the three-site model (Xu et al. 2013).

*: The H position in $Mg(OH)_{1.78}F_{0.22}$ is fixed the same as that for the natural sample.

[&]: The hydrogen occupancies are fixed during structure refinements, based on the EPMA results.

Table 4. The calculated bond lengths (Å) and bond angles (°) for the F-bearing brucite samples in both the single-site and three-site split-atom hydrogen models.

	$Mg(OH)_{1.78}F_{0.22}$	$Mg(OH)_{1.16}F_{0.84}$	$Mg(OH)_{1.99}F_{0.01}$
	single-site hydrogen model		
Mg-O(F)	2.0898(9)	2.0849(10)	2.0969(8)
O-H	0.9927(17)	1.06(10)	0.99(4)
Mg-O-H	119.75(4)	119.86(5)	119.83(3)
O(F)-Mg-O(F)	97.51(5)	97.37(6)	97.40(4)
O(F)…H	2.4927(11)	2.43(7)	2.49(3)
	three-site split-atom hydrogen model		
Mg-O(F)	2.0898(9)	2.0849(10)	2.0969(8)
O-H	1.035(2)	1.08(10)	1.03(4)
Mg-O-H	137.09(7)	130(10)	137(4)
O(F)-Mg-O(F)	97.51(5)	97.36(6)	97.40(4)
O(F)…H	2.623(1)	2.50(10)	2.63(3)

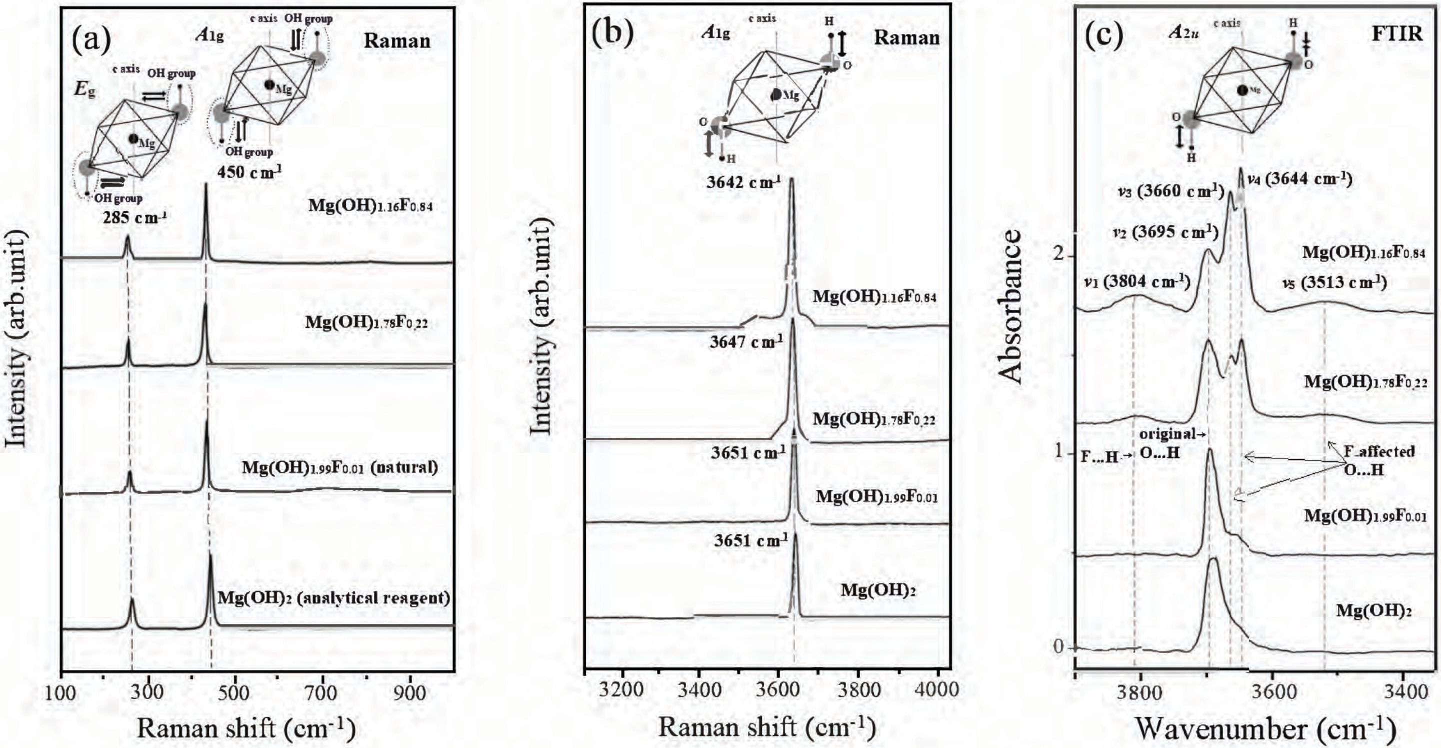
(a)
A_{1g}
Raman
c axis
OH group
E_g
Mg
450 cm^{-1}
285 cm^{-1}
$Mg(OH)_{1.16}F_{0.84}$
$Mg(OH)_{1.78}F_{0.22}$
$Mg(OH)_{1.99}F_{0.01}$ (natural)
$Mg(OH)_2$ (analytical reagent)
Intensity (arb.unit)
100
300
500
700
900
Raman shift (cm^{-1})
(b)
A_{1g}
c axis
H
O
Mg
Raman
3642 cm^{-1}
$Mg(OH)_{1.16}F_{0.84}$
3647 cm^{-1}
$Mg(OH)_{1.78}F_{0.22}$
3651 cm^{-1}
$Mg(OH)_{1.99}F_{0.01}$
3651 cm^{-1}
$Mg(OH)_2$
Intensity (arb.unit)
3200
3400
3600
3800
4000
Raman shift (cm^{-1})
(c)
A_{2u}
c axis
H
O
Mg
FTIR
ν_4 (3644 cm^{-1})
ν_3 (3660 cm^{-1})
ν_2 (3695 cm^{-1})
ν_1 (3804 cm^{-1})
ν_5 (3513 cm^{-1})
$Mg(OH)_{1.16}F_{0.84}$
$Mg(OH)_{1.78}F_{0.22}$
original→ O…H
F…H→
F_affected O…H
$Mg(OH)_{1.99}F_{0.01}$
$Mg(OH)_2$
Absorbance
0
1
2
3800
3600
3400
Wavenumber (cm^{-1})

Figure 1

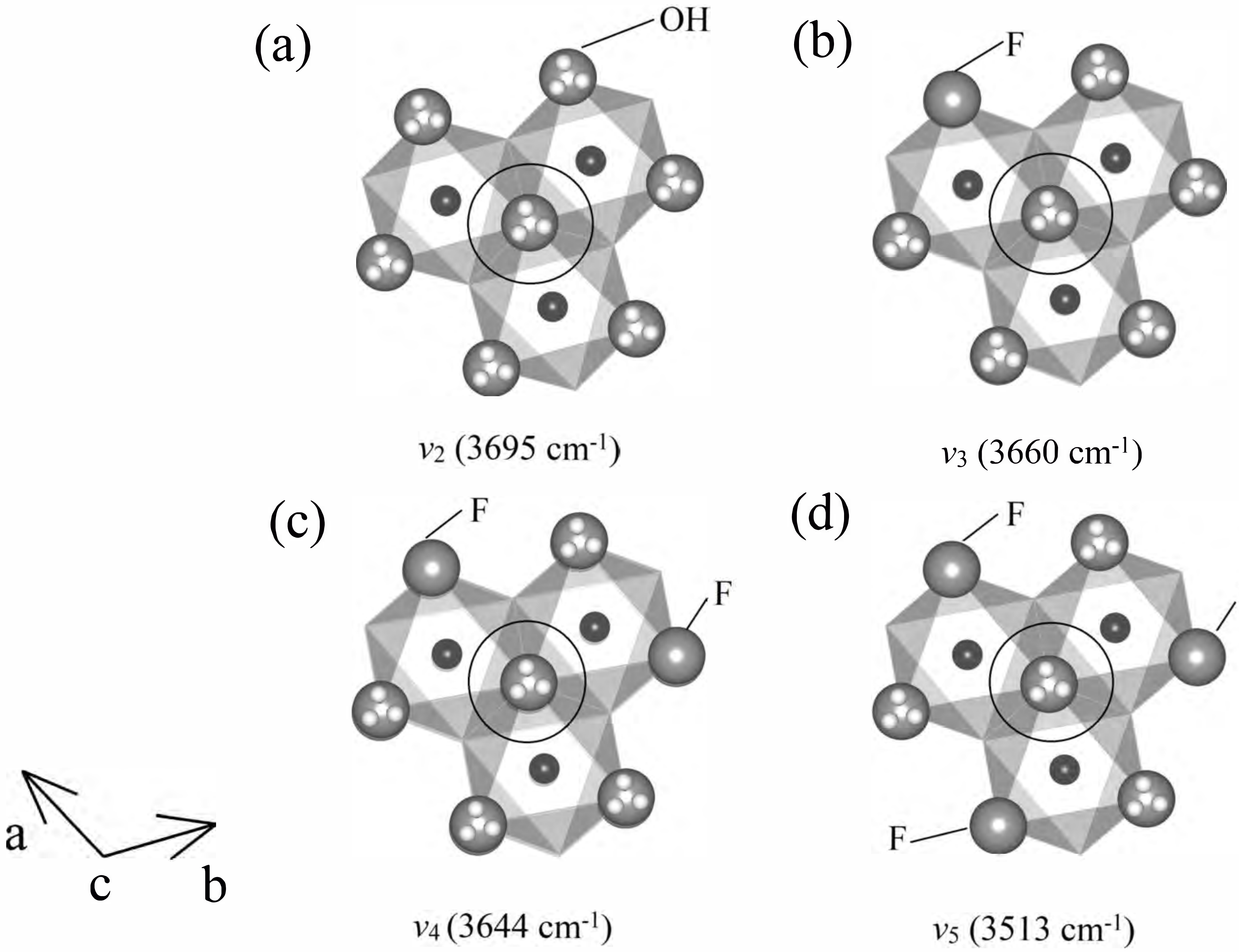
(a)
OH
ν_2 (3695 cm^{-1})
(b)
F
ν_3 (3660 cm^{-1})
(c)
F
F
ν_4 (3644 cm^{-1})
(d)
F
F
F
ν_5 (3513 cm^{-1})
a
c
b

Figure 2

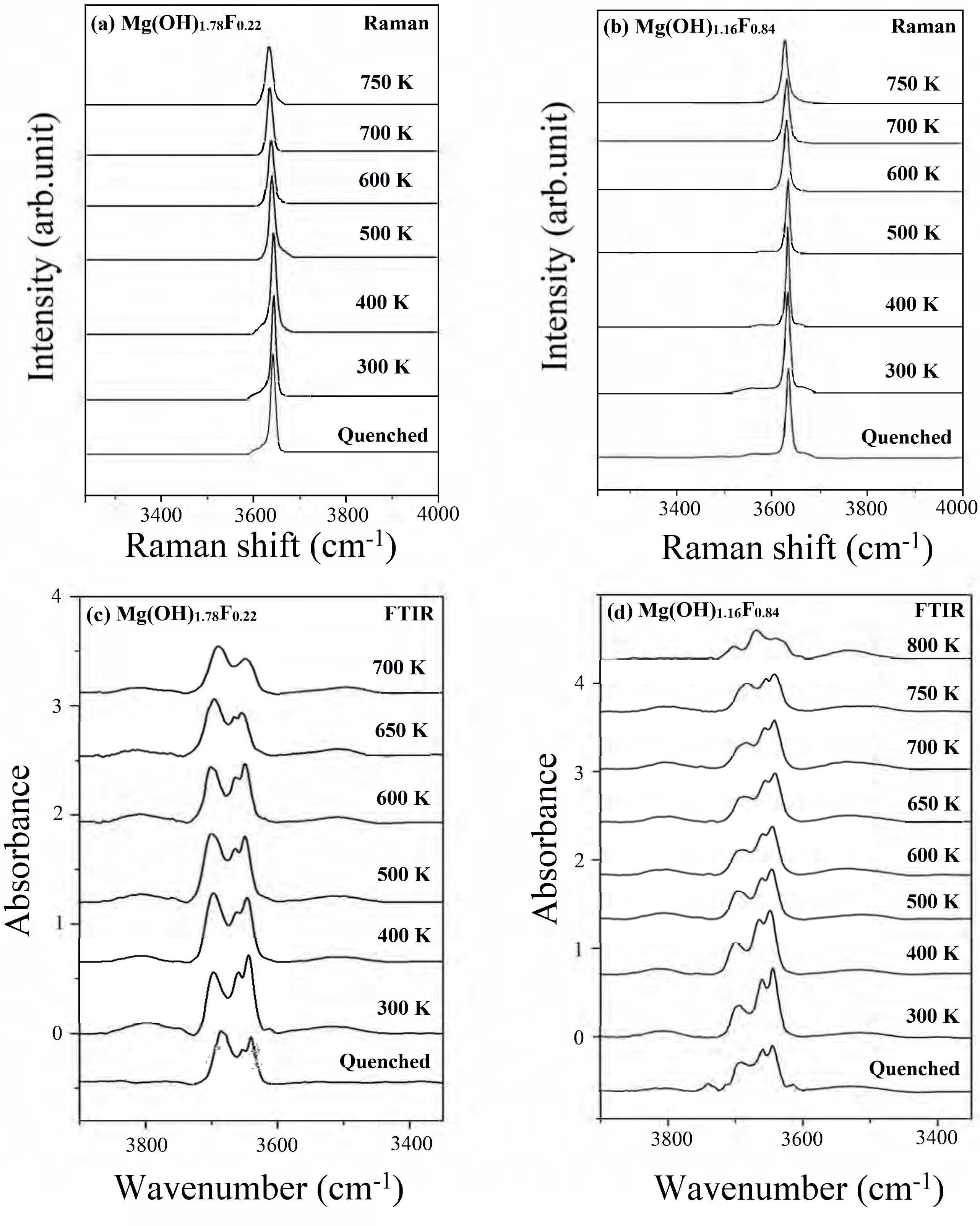
(a) Mg(OH)1.78F0.22
Raman
750 K
700 K
600 K
500 K
400 K
300 K
Quenched
Intensity (arb.unit)
3400
3600
3800
4000
Raman shift (cm-1)
(b) Mg(OH)1.16F0.84
Raman
750 K
700 K
600 K
500 K
400 K
300 K
Quenched
Intensity (arb.unit)
3400
3600
3800
4000
Raman shift (cm-1)
(c) Mg(OH)1.78F0.22
FTIR
700 K
650 K
600 K
500 K
400 K
300 K
Quenched
Absorbance
0
1
2
3
4
3800
3600
3400
Wavenumber (cm-1)
(d) Mg(OH)1.16F0.84
FTIR
800 K
750 K
700 K
650 K
600 K
500 K
400 K
300 K
Quenched
Absorbance
0
1
2
3
4
3800
3600
3400
Wavenumber (cm-1)

Figure 3

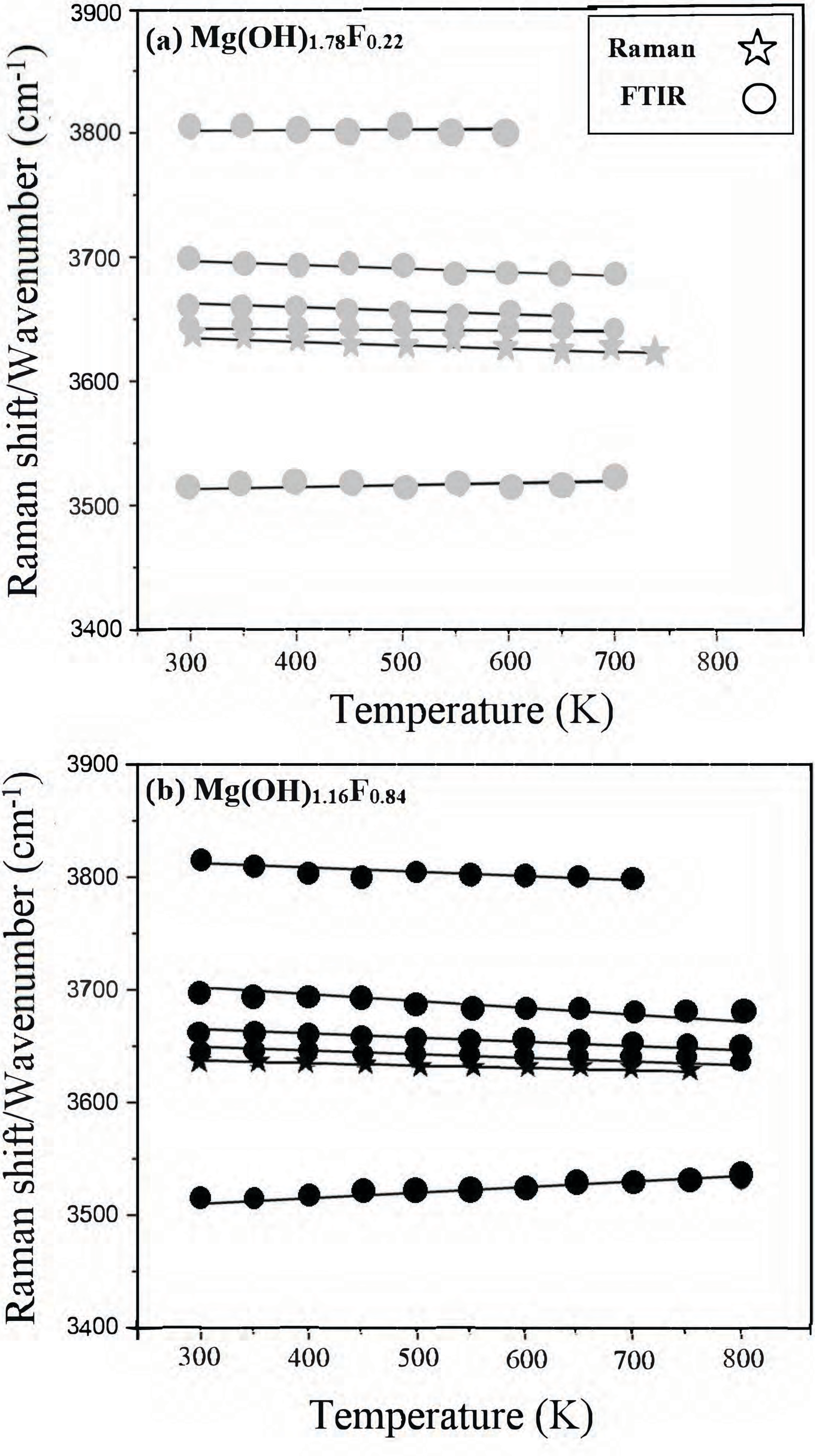
(a) $Mg(OH)_{1.78}F_{0.22}$
Raman
FTIR
Raman shift/Wavenumber (cm^{-1})
3900
3800
3700
3600
3500
3400
300
400
500
600
700
800
Temperature (K)
(b) $Mg(OH)_{1.16}F_{0.84}$
Raman shift/Wavenumber (cm^{-1})
3900
3800
3700
3600
3500
3400
300
400
500
600
700
800
Temperature (K)

Figure 4

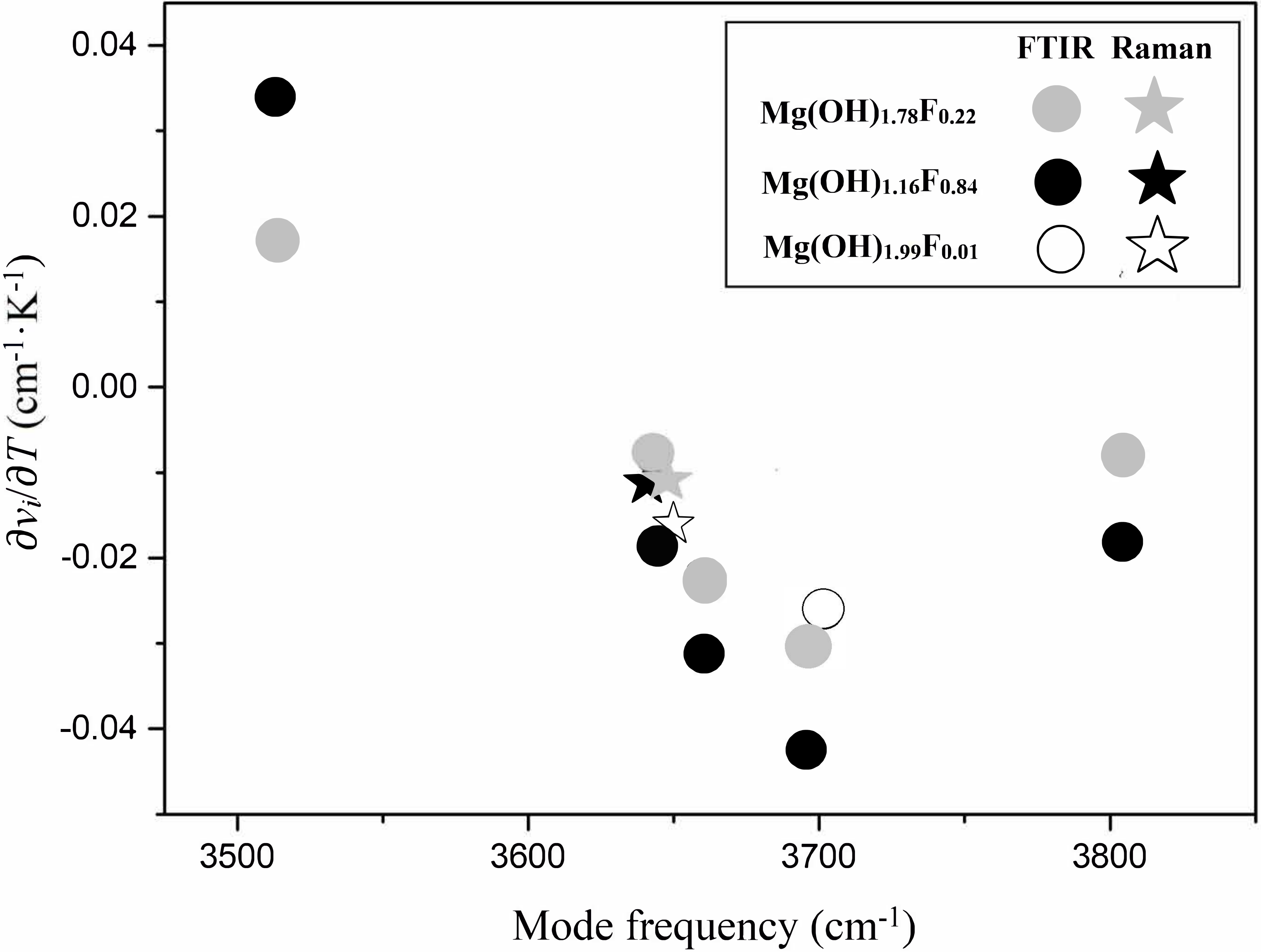
FTIR
Raman
Mg(OH)1.78F0.22
Mg(OH)1.16F0.84
Mg(OH)1.99F0.01
0.04
0.02
0.00
-0.02
-0.04
∂νi/∂T (cm-1·K-1)
3500
3600
3700
3800
Mode frequency (cm-1)

Figure 5

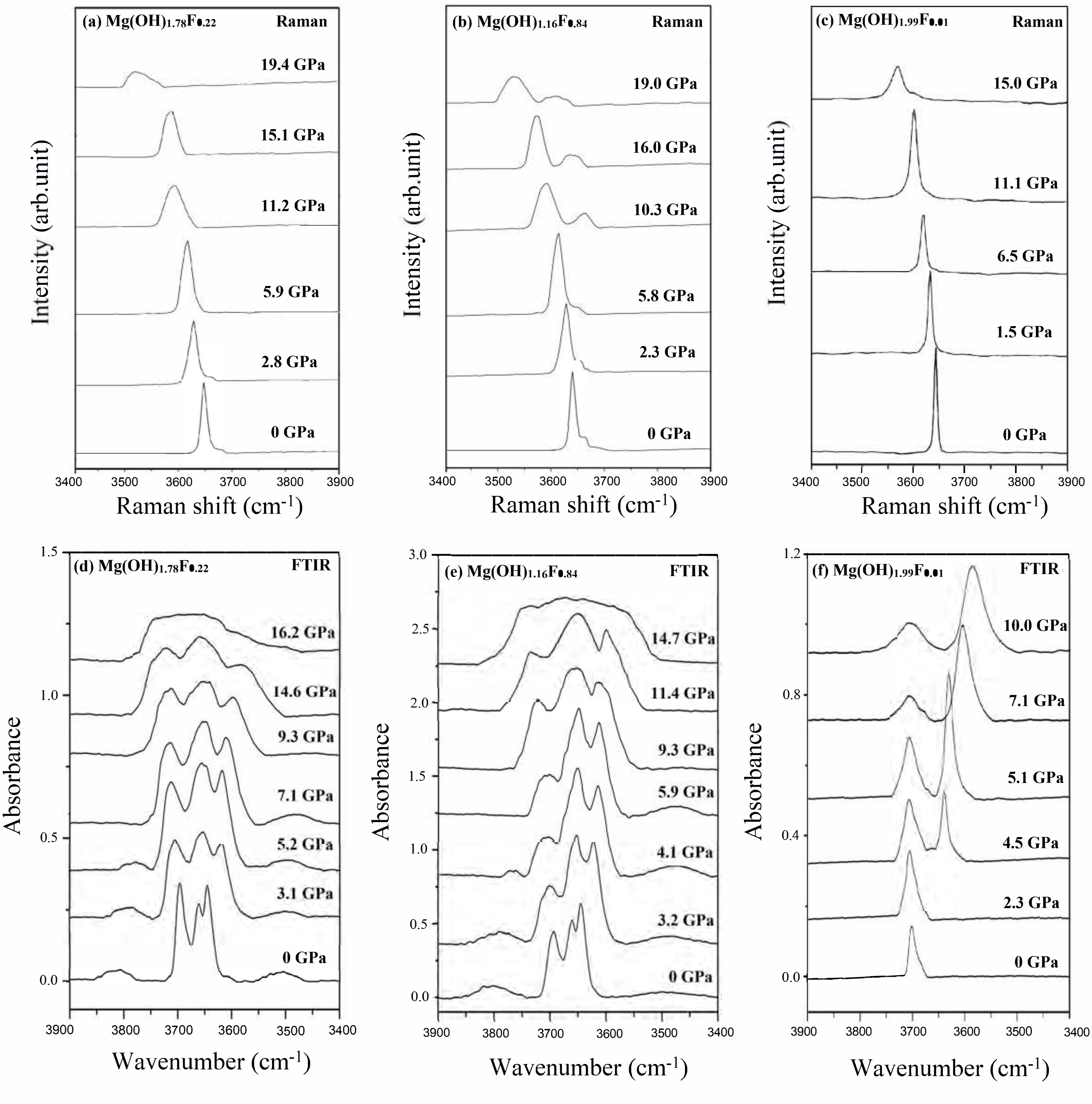

(a) Mg(OH)1.78F0.22
Raman
19.4 GPa
15.1 GPa
11.2 GPa
5.9 GPa
2.8 GPa
0 GPa
Intensity (arb.unit)
Raman shift (cm-1)
3400
3500
3600
3700
3800
3900
(b) Mg(OH)1.16F0.84
Raman
19.0 GPa
16.0 GPa
10.3 GPa
5.8 GPa
2.3 GPa
0 GPa
(c) Mg(OH)1.99F0.01
Raman
15.0 GPa
11.1 GPa
6.5 GPa
1.5 GPa
0 GPa
(d) Mg(OH)1.78F0.22
FTIR
16.2 GPa
14.6 GPa
9.3 GPa
7.1 GPa
5.2 GPa
3.1 GPa
0 GPa
Absorbance
Wavenumber (cm-1)
0.0
0.5
1.0
1.5
(e) Mg(OH)1.16F0.84
FTIR
14.7 GPa
11.4 GPa
9.3 GPa
5.9 GPa
4.1 GPa
3.2 GPa
0 GPa
0.0
0.5
1.0
1.5
2.0
2.5
3.0
(f) Mg(OH)1.99F0.01
FTIR
10.0 GPa
7.1 GPa
5.1 GPa
4.5 GPa
2.3 GPa
0 GPa
0.0
0.4
0.8
1.2

Figure 6

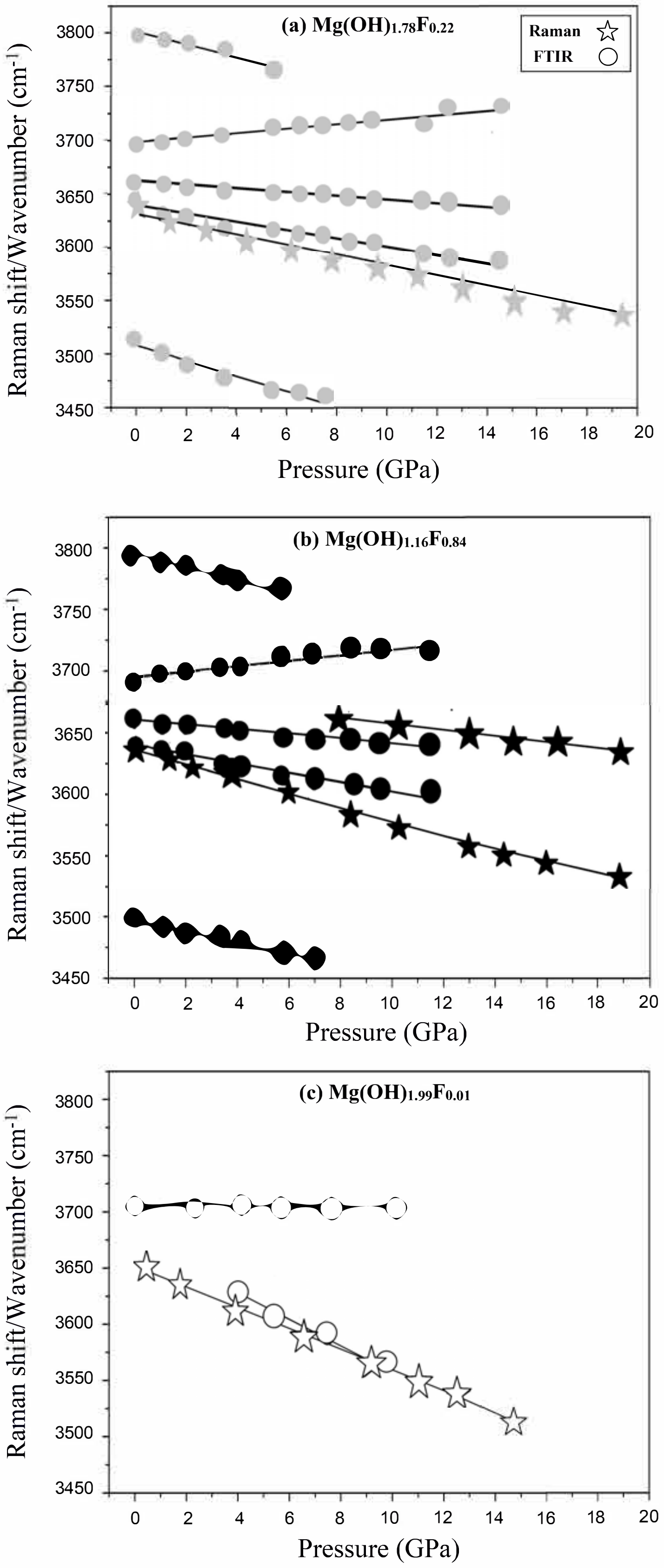
(a) $Mg(OH)_{1.78}F_{0.22}$
Raman ☆
FTIR ○
(b) $Mg(OH)_{1.16}F_{0.84}$
(c) $Mg(OH)_{1.99}F_{0.01}$
Raman shift/Wavenumber (cm^{-1})
3450
3500
3550
3600
3650
3700
3750
3800
Pressure (GPa)
0
2
4
6
8
10
12
14
16
18
20

Figure 7

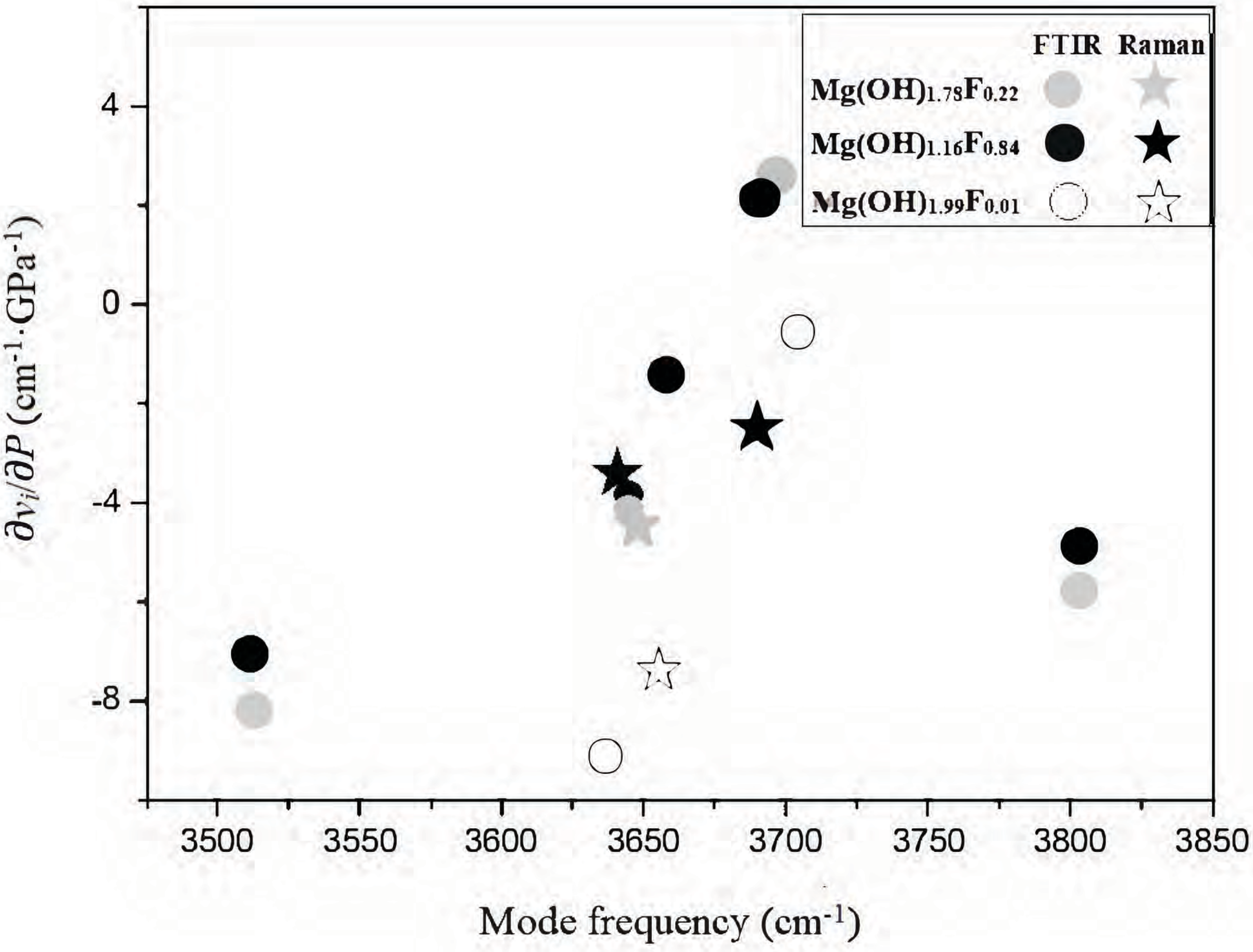

FTIR
Raman
Mg(OH)1.78F0.22
Mg(OH)1.16F0.84
Mg(OH)1.99F0.01
4
0
-4
-8
3500
3550
3600
3650
3700
3750
3800
3850
∂νi/∂P (cm-1·GPa-1)
Mode frequency (cm-1)

Figure 8